ISSN: 0003-6935

Applied Optics

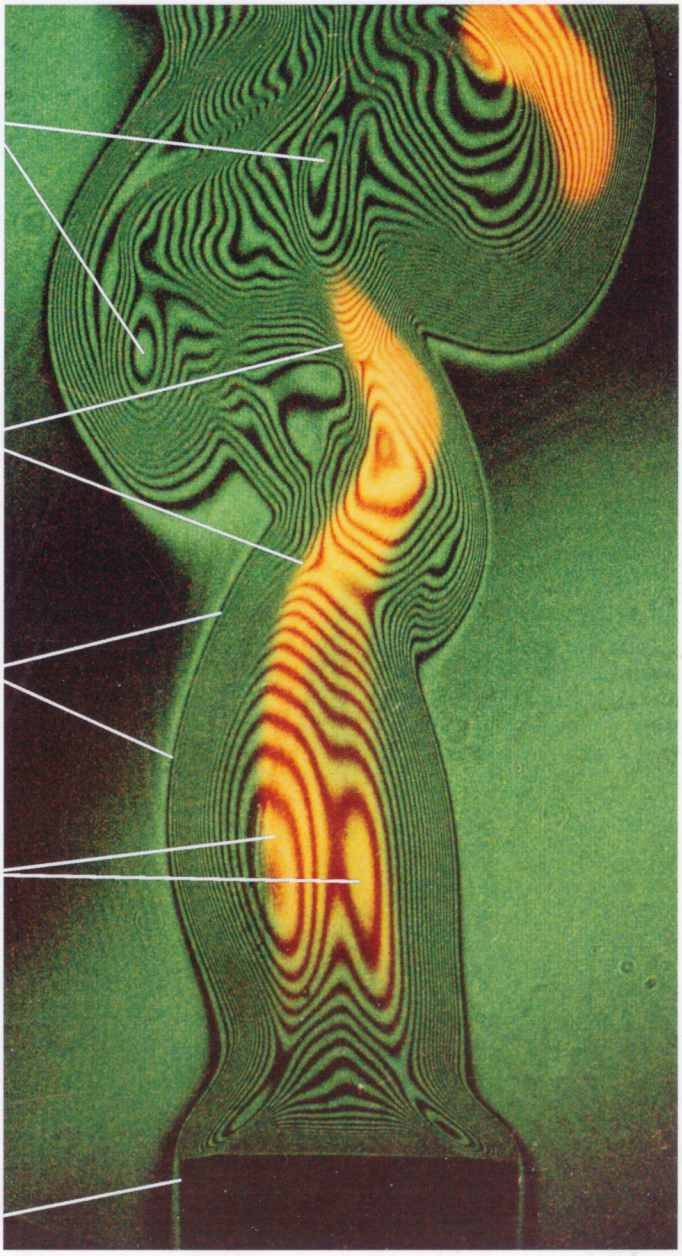

$d = 50$ mm

OSA®
The Optical Society

10 August 2009

Determining the effect of species composition on temperature fields of tank flames using real-time holographic interferometry

Markus Gawlowski,[1] Kerry E. Kelly,[2] Laurie A. Marcotte,[2] and Axel Schönbucher[1,*]

[1]Institute for Chemical Engineering I, University of Duisburg-Essen, Universitaetsstrasse 5, 45117 Essen, Germany

[2]Department for Chemical Engineering, University of Utah, 3290 MEB, 50 South Central Campus Drive, Salt Lake City, 84112, USA

*Corresponding author: axel.schoenbucher@uni-due.de

Received 13 April 2009; revised 20 July 2009; accepted 22 July 2009; posted 22 July 2009 (Doc. ID 109923); published 4 August 2009

Interference fringe fields and the visible flame field of a 50 mm diameter n-hexane tank flame were simultaneously measured using a real-time holographic interferometer with special image optics. An inhouse developed image processing method was applied to the holographic images to calculate the interference fringe order profiles. The effect of species composition on temperature profiles was studied by considering three different cases: using the measured species profiles, using an overall reaction mechanism based on stoichiometric combustion, and by assuming that the flame consists of hot air. The results show that species composition has the largest effect on temperature fields in regions near the flame axis at lower axial distances. In the region of the plume zone, the flame consists primarily of hot air due to the increase in total entrained air.

OCIS codes: 090.5694, 100.2000, 120.1740, 120.2880, 120.6780, 280.2470.

1. Introduction

Nonpremixed tank and pool fires can occur during the transportation or storage of hazardous materials, e.g., liquid hydrocarbon fuels, which can potentially lead to loss of life and extensive property damage [1]. A large buoyancy-driven fire consists of three different flow regions [1,2]. The lower clear burning zone is characterized by a luminous zone, while the transition or pulsation zone consists of flame pockets that emerge from the clear burning zone. The upper plume zone contains almost no luminous zones [3]. In tank and pool fires, organized structures exist [4] and have been studied for a better understanding of buoyancy-driven nonpremixed fires [4].

The knowledge of temperatures within such fires is of great interest for calculating, e.g., the heat transfer to neighboring or impinging objects [5]. The thermal radiation from a fire and the thermal separation distances are dependent not only on the flame temperature but also on the concentrations of soot, CO_2, and H_2O, as well as the view factor (size, shape, orientation, and distance from the fire) [1,6].

A first step toward understanding large buoyancy-driven, nonpremixed flames is to study laboratory-scale tank flames. Thermocouples are a widely used method for temperature measurements in flames [7,8]. This technique provides pointwise measurements but disturbs the flow and temperature field of the flame [5,7–9]. Because of the large time constant of thermocouples, it is not possible to measure instantaneous temperatures in a flame. A more recent method is the application of holographic interferometry (HI). HI is a nonintrusive and inertialess diagnostic technique that provides high temporal and spatial resolution without disturbing the flame [5,9–18]. HI is not restricted to pointwise measures like thermocouples, and it provides information about the three-dimensional (3D) flame field by

0003-6935/09/234625-12$15.00/0

using a multidirectional holographic interferometer in nonaxisymmetric turbulent flames [11]. HI can be applied as a real-time method or as a discontinuous double-exposure technique [19]. By using a high-speed camera and special image optics, the simultaneous recording of the interferogram and the visible flame field can be recorded. With this technique it is also possible to analyze correlations between the oscillations of the interference fringes of the thermal boundary layer and the puffing frequency of the visible flame [4].

Fuel and air mix during the combustion process in nonpremixed tank flames. Different types of fuel require different quantities of oxygen for their stoichiometric (complete) combustion. In general, the higher fuel carbon numbers require higher oxygen concentrations for stoichiometric combustion. The type of combustion is classified by the equivalence ratio Φ and has a range between 0 (air) $< \Phi < \infty$ (fuel):

$$\Phi = \frac{(\tilde{\gamma}_{\text{air}}/\tilde{\gamma}_f)_s}{\tilde{\gamma}_{\text{air}}/\tilde{\gamma}_f}, \tag{1}$$

where $\tilde{\gamma}_{\text{air}}$ and $\tilde{\gamma}_f$ are the mole fractions of air and fuel, respectively, and s denotes stoichiometric combustion. An equivalence ratio of $\Phi = 1$ denotes stoichiometric combustion, $\Phi > 1$ denotes fuel rich combustion, and $\Phi < 1$ denotes fuel lean combustion.

When flame temperatures are determined from the refractive index field, the composition of the reactants, combustion products, and consequently the equivalence ratio Φ, should be determined. If the species composition is unknown, a relationship between the calculated mixture fraction and the Gladstone–Dale equation can be used [9].

In premixed lean flames with $\Phi < 1$, the effect of changes in species composition on flame temperatures is much smaller than the effect of density or temperature changes and is therefore often neglected [5,7,9,11–13,17]. Tieng *et al.* [13] showed that the effect of species composition is less significant for premixed lean flames than for premixed rich and nonpremixed flames. In premixed lean flames it is assumed that the fuel mixture is burned under stoichiometric conditions, so the species composition of the combustion products can be calculated. For nonpremixed flames this assumption is not valid. In the approximately nonreacting plume region of nonpremixed flames, the refractive index field is approximately that of hot air.

The axisymmetric refractive index field of flames can be calculated by using the Abel transformation [19,20]. The Abel transformation is valid for axisymmetric phase objects, e.g., in the lower region of tank flames, and assumes that the refractive index gradient is small along the light path [20]. The change in refraction along the light path in this region leads to small errors in evaluation of the interferograms and is discussed in [15]. If the light rays are projected back to the center plane by the imaging system, the deflection of the light ray is negligible [21]. Three criteria can be used to estimate the amount of the deflection of the light ray as discussed in [22]: the occurrence of schlieren, or localized differences in the optical path length; the presence of acute-angled redirections of interference fringes; and the identification of a large number of irresolvable interference fringes caused by large refractive index gradients or large optical path lengths. According to the above mentioned criteria, light rays are not deflected in the approximately axial symmetric region of the tank flame. In the case of nonpremixed tank flames, large refractive index gradients are formed mainly in the relatively cold vaporizing fuel region above the fuel surface. The assumption of a constant refractive index along the light path is valid only for two-dimensional (2D) phase objects, whereas in asymmetric 3D phase objects the laser's light rays are partly deflected along the light path.

Temperature measurements based on HI have been carried out for laminar premixed gaseous flames [5,7,10,14,15,23]; these neglect the dependence of species composition on the refractive index. They have also been performed on laminar nonpremixed gaseous flames, and these consider the species composition effect [10,11,13,16,18,23]. The purpose of this study is to show the influence of species composition on the temperature field for a turbulent nonpremixed tank flame at different heights above the rim.

2. Physical Interpretation of the Interference Fringe Pattern for Phase Objects

A detailed description of HI and its application for obtaining the refractive index field of flames can be found in [18–20,23–25]. Figure 1 presents an example interferogram of a small scale n-hexane tank flame showing different organized structures. The interference fringe pattern is correlated with the integral over the optical light path difference. An interference fringe represents a line of constant refractive index difference along the light path z and is expressed as multiples of S [S denotes the interference fringe order, $S = \pm(j-1)/2, j = 2, 3, \ldots$] of the laser wavelength λ:

$$S(x,y,t)\lambda = \int_{-z(y)}^{z(y)} [n_m(x,y,z,t) - n_a]\mathrm{d}z, \tag{2}$$

where $n_a = 1.003$ is the refractive index of ambient air, n_m is the refractive index of the flame–gas mixture, and z is the coordinate in the direction of the light path through the visible flame including the thermal boundary layer.

The Abel inversion technique [19,20,24] was used to obtain the refractive index profiles $n_m(r,x,t)$ of the flame–gas mixture from the first derivative $(\partial S/\partial y)$ of the interference fringe order:

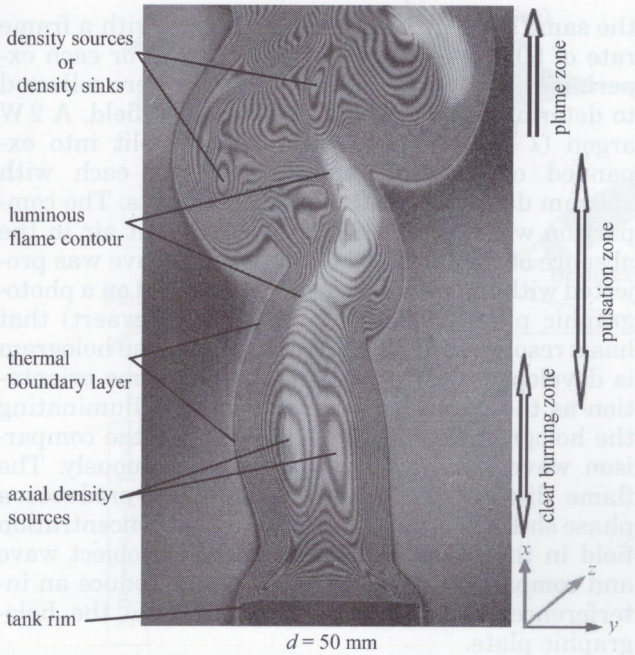

Fig. 1. (Color online) Interferogram of an n-hexane tank flame ($d = 50$ mm) superimposed simultaneously with the visible luminous flame contour showing also different flow regions, e.g., density sources and sinks and thermal boundary layer.

$$n_m(r,x,t) - n_a = -\frac{\lambda}{\pi}\int_r^R \frac{\partial S(x,y,t)/\partial y}{\sqrt{y^2-r^2}}\mathrm{d}y, \tag{3}$$

where r is the radial coordinate and R is the radius of the flame including the thermal boundary layer. The radial refractive index profiles $n_m(r,x,t)$ were obtained using a step function with 24 steps [20]. The axisymmetric refractive index field was divided into a finite number of equally spaced circular bands with $\Delta r = 1$ mm. It was assumed that n_m was constant along the light path and that the laser beam passed through the temperature field without refraction. Therefore the geometric path length through each circular band was known. If the refractive index field $n_m(r,x,t)$ is determined, the density field $\rho_m(r,x,t)$ of the flame–gas mixture can be calculated using the Gladstone–Dale relationship with the following modification [4]:

$$\rho_m(r,x,t) = \frac{2}{3}[n_m(r,x,t) - 1]\frac{1}{\bar{N}_m}, \tag{4a}$$

with

$$\bar{N}_m(r,x) = \frac{\sum_i \bar{\gamma}_i(r,x)N_{i,0}}{\sum_i \bar{\gamma}_i(r,x)}, \tag{4b}$$

where $\bar{N}_m$ is the time-averaged refractivity of the flame–gas mixture, $N_{i,0}$ is the specific standard refraction of the stable species i, and $\bar{\gamma}_i$ is the time-averaged mass fraction of the stable species i. Using the ideal gas law, the flame temperature field $T_m(r,x,t)$ can then be calculated by the equation

$$T_m(r,x,t) = \frac{1}{\rho_m(r,x,t)}\frac{\sum_i \bar{\gamma}_i(r,x)\rho_{i,0}}{\sum_i \bar{\gamma}_i(r,x)}T_0 \tag{5}$$

or with Eqs. (3), (4a), (4b), and (5),

$$T_m(r,x,t) = \frac{3/2}{-\frac{\lambda}{\pi}\int_r^R \frac{\partial S(x,y,t)/\partial y}{\sqrt{y^2-r^2}}\mathrm{d}y + n_a - 1} \times \frac{\sum_i \bar{\gamma}_i(r,x)\rho_{i,0}\sum_i \bar{\gamma}_i(r,x)N_{i,0}}{[\sum_i \bar{\gamma}_i(r,x)]^2}T_0, \tag{6}$$

where $\rho_{i,0}$ denotes the standard density of the species i, and T_0 is the temperature at standard conditions ($T_0 = 273$ K). From Eqs. (4)–(6) it can be seen that ρ_m and T_m depend principally on the mass fraction γ_i of the stable chemical species i.

If the local composition is assumed to be that of pure air ($\gamma_i = \gamma_{\mathrm{air}} = 1$), Eq. (6) becomes

$$T_m(r,x,t) = \frac{3/2\rho_{i,0}N_{i,0}T_0}{-\frac{\lambda}{\pi}\int_r^R \frac{\partial S(x,y,t)/\partial y}{\sqrt{y^2-r^2}}\mathrm{d}y + n_a - 1}, \tag{7}$$

with $i =$ air.

If the chemical species are measured by gas chromatography (GC), only time-averaged values of the volume fractions $\bar{\gamma}_{v,i}$ or mass fractions $\bar{\gamma}_i$ can be obtained, because GC measurements have a large time scale ($\Delta t < 10$ s) compared to the time scale of the measured refractive index ($\Delta t \approx 1/2500$ s). This has the consequence that *quasi*-instantaneous density or flame temperatures fields can be calculated.

An error analysis was performed on the final flame temperature as described by Ibarreta *et al.* [26]. The error on the final flame temperature involved in using Eq. (7) is related to the nonlinear relationship between the refractive index and temperature field. With the following simplification $\delta = n_m(r,x,t) - 1$ in Eq. (7), the error ΔT_m becomes

$$|\Delta T_{\mathrm{m}}| = \frac{T_{\mathrm{m}}^2}{3/2\rho_{i,0}N_{i,0}T_0}|\Delta\delta|. \tag{8}$$

Equation (8) shows that the error on flame temperature ΔT_m depends on T_m^2. The error that arises from the Abel inversion Eq. (3) on the final flame temperature must also be evaluated. For this purpose, the right-hand side of Eq. (3) is considered as the variable $\eta = n_m(r,x,t) - n_a$:

$$\eta = n_m(r,x,t) - n_a \approx \delta - \delta_a. \tag{9}$$

If, e.g., δ_a is not accurately known, it is possible to generalize Eq. (9) by selecting another reference point, so that the change in δ becomes

$$\eta - \eta_{\mathrm{ref}} \approx \delta - \delta_{\mathrm{ref}}, \quad (10)$$

with

$$\delta = (n-1) \approx \eta - \eta_{\mathrm{ref}} + \delta_{\mathrm{ref}}, \quad (11)$$

where δ_{ref} is $n_m(r,x,t) - 1$ at the reference point and η_{ref} is the value of the Abel inversion at this point. The refractive index or the temperature must be accurately known at this reference point; otherwise, the reference value gives an error in δ_{ref} that will propagate to δ and finally to the flame temperature.

Taking all of this into account, the error in determining the refractive index at any point results in

$$|\Delta\delta| = |\Delta(\eta - \eta_{\mathrm{ref}})| + |\Delta\delta_{\mathrm{ref}}| = |\Delta\eta'| + |\Delta\delta_{\mathrm{ref}}|, \quad (12)$$

where $\Delta\eta'$ is the error from the Abel inversion over the radial coordinate, while $\Delta\delta_{\mathrm{ref}}$ shows the error in determining the refractive index of the reference point. Combining Eqs. (8) and (12), an error on the final flame temperature $T_m(r,x,t)$ can be obtained by

$$|\Delta T_m| = \underbrace{\frac{T_m^2}{3/2\rho_{i,0}N_{i,0}T_0}|\Delta\eta'|}_{\Delta T_{m1}} + \underbrace{\left(\frac{T_m}{T_{\mathrm{ref}}}\right)^2|\Delta T_{\mathrm{ref}}|}_{\Delta T_{m2}}, \quad (13)$$

where the first term on the right-hand side represents the error of the Abel inversion, and the second term is the error in determining the reference temperature (e.g., with thermocouples). Based on the second term, the error on flame temperature is $\Delta T_{m2} = 76\,\mathrm{K}$ if a flame temperature of $T_m = 1500\,\mathrm{K}$ is chosen, and $T_{\mathrm{ref}} = T_a = 298\,\mathrm{K}$ with an error in ΔT_{ref} of 3 K (1% error). To reduce the error in flame temperature, it is necessary to obtain a reference value near the flame temperature by reducing $(T_m/T_{\mathrm{ref}})^2$. According to Hauf *et al.* [20], the presented method of the Abel inversion has a mean error of 5% on the calculation of the refractive index n_m. This results in an error of the Abel inversion on flame temperature of $\Delta T_{m1} = 48\,\mathrm{K}$ for $T_m = 1500\,\mathrm{K}$. The final error on flame temperature is $\Delta T_m = \Delta T_{m1} + \Delta T_{m2} = 124\,\mathrm{K}$ (9%).

3. Experiment

A. Holographic Mach–Zehnder Interferometry

In this investigation the density and temperature field in a nonpremixed, 50 mm diameter n-hexane flame were measured using real-time HI. The steel tank was continuously supplied from an n-hexane reservoir, and the fuel level was kept constant at 2 mm below the tank rim. The mass burning rate of n-hexane was $\dot{m}_f'' = 0.024\,\mathrm{kg/(m^2s)}$, and the volumetric flow rate of n-hexane was adjusted to $\dot{V}_f = 0.06\,\mathrm{ml/s}$ at a constant temperature of $T = 293\,\mathrm{K}$. Figure 2(a) shows the holographic Mach–Zehnder interferometer setup. In this study the interferogram and the visible flame field were recorded simultaneously at the same scale by a high-speed camera with a frame rate of 500 fps (Ektapro 4540, Kodak). For each experiment, approximately 4000 images were collected to determine the averaged fringe order field. A 2 W argon ($\lambda = 514.5\,\mathrm{nm}$) laser beam is split into expanded object and reference beams, each with 250 mm diameters and plane wave fronts. The comparison wave front refers to the ambient air in the absence of the flame. The comparison wave was projected with the reference beam and stored on a photographic plate (Holotest 10E56, Agfa-Gevaert) that has a resolution of ~2000 fringes/mm. The hologram is developed and repositioned in the same orientation as the comparison wave front. By illuminating the hologram with the reference beam, the comparison wave can be reconstructed continuously. The flame distorts the wave fronts, which produces a phase shift due to the temperature and concentration field in the flame. When the real-time object wave and comparison wave interfere, they produce an interference fringe pattern projected onto the holographic plate.

B. Image Optics

With the optical setup in Fig. 2(b) the interference fringe field and the visible flame field of the n-hexane flame were simultaneously recorded at the same scale and time. For this purpose, the lens of the high speed camera was replaced by a lens system (achromat) that projected the interferogram and the visible flame at the same scale on the film plane. Therefore a synchronous assignment of the instantaneous interferogram and the instantaneous visible flame field was achieved. To obtain a good contrast between the two images, the intensity ratio of the object and reference beams was adjusted by gray filters that are located within both laser beams.

An error analysis has shown that the total error of the very high-quality image optics is caused by several factors, including light diffraction, spherical and chromatic aberrations, astigmatism, coma, field curvature, and distortion. These errors have been corrected so that the shifting of the interference fringes was smaller than the measured displacements of the evaluated interference fringes.

C. Gas Chromatographic Measurements

In order to examine the species composition effect in the n-hexane flame, the concentrations of the species i were measured by a gas chromatograph (F22, Perkin Elmer) and were expressed as volume fractions $\bar{\gamma}_{v,i}$. The following relationship between the measured volume fractions $\bar{\gamma}_{v,i}$ and calculated mass fractions $\bar{\gamma}_i$ exists:

$$\bar{\gamma}_i = \frac{\bar{\gamma}_{v,i}\tilde{M}_i}{\sum_i \bar{\gamma}_{v,i}\tilde{M}_i}, \quad (14)$$

where $\tilde{M}_i$ is the molar mass of the species i.

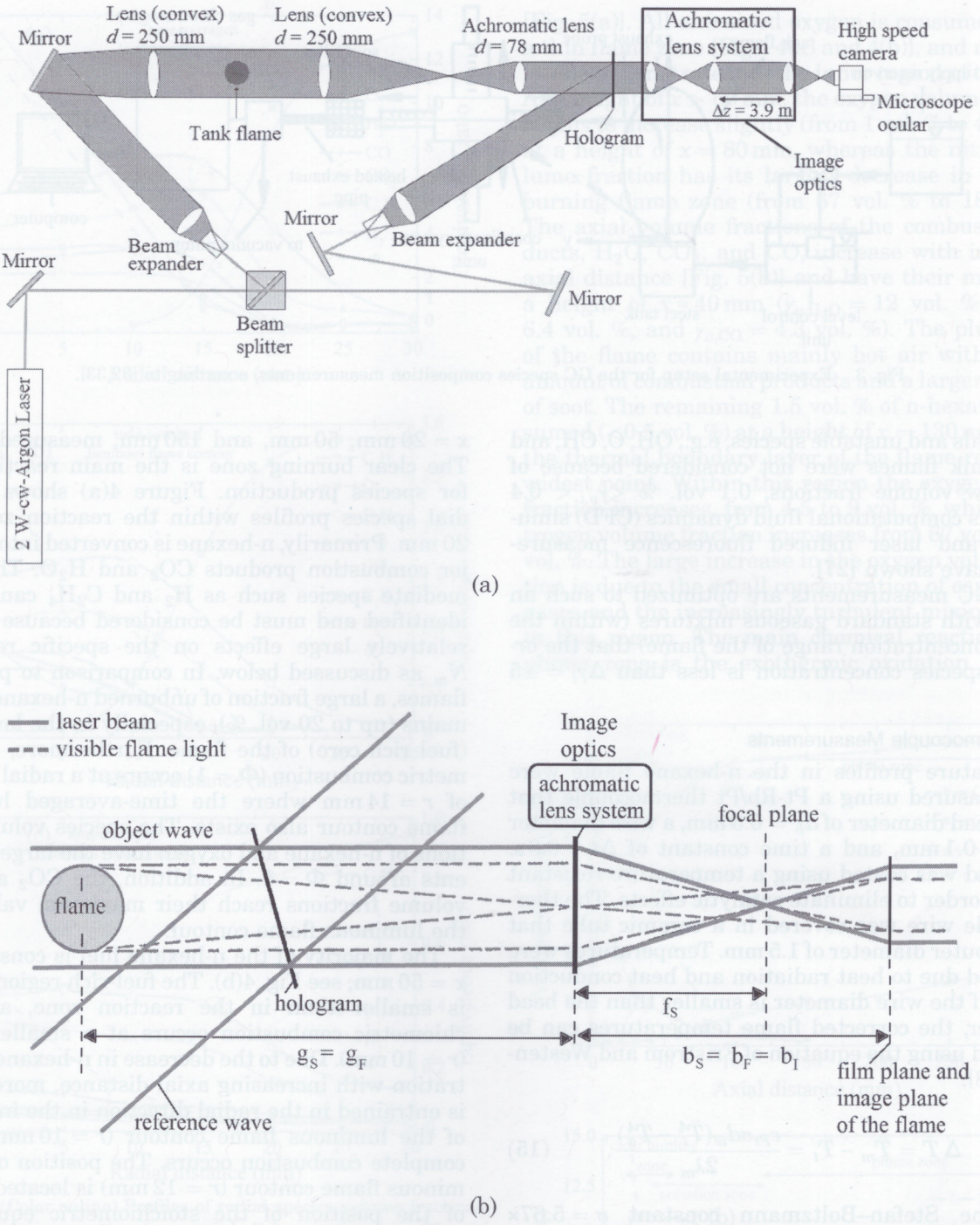

Fig. 2. (Color online) (a) High-speed holographic real-time interferometer (Mach–Zehnder) with a 250 mm beam expanding including the image optics, according to [4,22]. (b) Optical setup for the simultaneous recording of the intereference fringe field and the visible flame field (f_S, focal length; g_S, g_F, object distance for the interferogram, object distance of the flame, respectively; b_S, b_F, b_I, image length of the recording optics, flame, interferogram, respectively).

A low temperature GC setup (Fig. 3) was used for measuring the stable species with a volume fraction $\bar{\gamma}_{v,i}$ of >0.05 vol. %. The measured time-averaged data for the eight major species (CO_2, H_2O, CO, CH_4, C_2H_4, N_2, O_2, and H_2) have a total concentration of 95.5 vol. % [Figs. 4(a)–4(c), 5(a), and 5(b)], and the nine minor species (Ar, C_2H_6, C_2H_2, C_3H_8, C_3H_6, C_4H_{10}, C_4H_8, C_5H_{12}, and C_6H_6) have a total concentration of 4 vol. %. Identification of the characteristic peaks from the resulting chromatograms was performed by a computer aided system.

Flame gas samples were taken across the width of the flame at different axial distances ranging from 20 mm to 300 mm above the tank rim. The mass fractions of each species i were then determined through the knowledge of their molar mass, from Eq. (14).

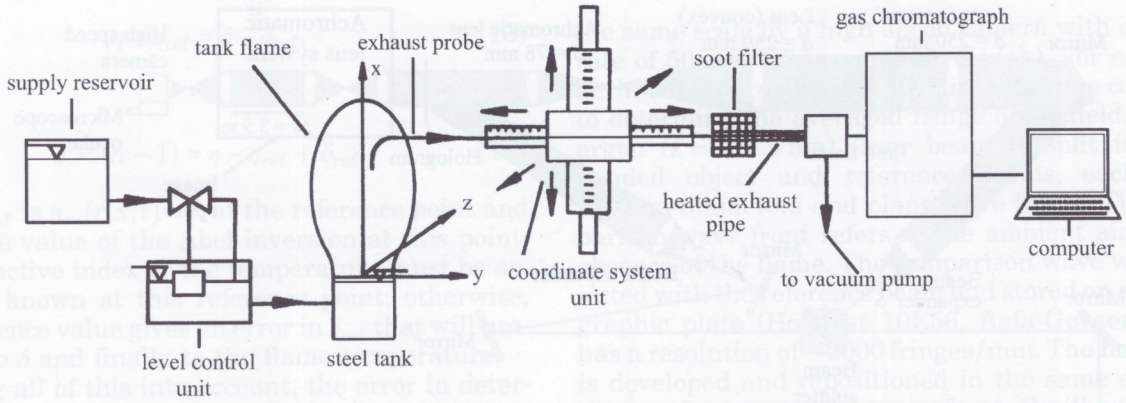

Fig. 3. Experimental setup for the GC species composition measurements, according to [32,33].

Radicals and unstable species, e.g., OH, O, CH, and N, in tank flames were not considered because of their low volume fractions, 0.1 vol. % $<\bar{\gamma}_{v,i}<$ 0.4 vol. %, as computational fluid dynamics (CFD) simulations and laser induced fluorescence measurements have shown [27].

The GC measurements are optimized to such an extent with standard gaseous mixtures (within the whole concentration range of the flame) that the error on species concentration is less than $\Delta\bar{\gamma}_i = \pm 5$ vol. %.

D. Thermocouple Measurements

Temperature profiles in the n-hexane flame were also measured using a Pt-Rh/Pt thermocouple that had a bead diameter of $d_b = 0.3$ mm, a wire diameter of $d_w = 0.1$ mm, and a time constant of $\Delta t = 0.8$ s. The bead was coated using a temperature resistant SiO_2 in order to eliminate catalytic effects. The thermocouple wire was covered in a ceramic tube that had an outer diameter of 1.5 mm. Temperatures were corrected due to heat radiation and heat conduction losses. If the wire diameter is smaller than the bead diameter, the corrected flame temperatures can be obtained using the equation of Fristrom and Westenberg [28]:

$$\Delta\bar{T} = \bar{T}_m - \bar{T}_t = \frac{\varepsilon_{Pt}\sigma d_w(\bar{T}_t^4 - T_a^4)}{2\lambda_m}, \qquad (15)$$

with the Stefan–Boltzmann constant $\sigma = 5.67\times 10^{-8}$ W/(m^2 K^4), the emissivity of platinum ε, the diameter of the wire d_w, the measured temperature with the thermocouple T_t, the ambient temperature $T_a = 298$ K, and the heat conduction of the flame gas mixture λ_m.

4. Results and Discussion

A. Radial and Axial Species Concentration Profiles

In the following section, axial and radial species volume fraction profiles are discussed together with the visible luminous flame contour.

Figures 4(a)–4(c) present profiles of radial species volume fractions at different axial positions, $x = 20$ mm, 50 mm, and 150 mm, measured by GC. The clear burning zone is the main reaction zone for species production. Figure 4(a) shows the radial species profiles within the reaction zone, $x =$ 20 mm. Primarily, n-hexane is converted into the major combustion products CO_2 and H_2O. The intermediate species such as H_2 and C_2H_4 can also be identified and must be considered because of their relatively large effects on the specific refraction N_m as discussed below. In comparison to premixed flames, a large fraction of unburned n-hexane fuel remains (up to 20 vol. %), especially in the lower part (fuel rich core) of the flame. Furthermore, stoichiometric combustion ($\Phi = 1$) occurs at a radial position of $r = 14$ mm where the time-averaged luminous flame contour also exists. The species volume fractions of n-hexane and oxygen have the largest gradients around $\Phi = 1$. In addition, the CO_2 and H_2O volume fractions reach their maximum value near the luminous flame contour.

The majority of the n-hexane fuel is consumed at $x = 50$ mm; see Fig. 4(b). The fuel-rich region ($\Phi > 1$) is smaller than in the reaction zone, and stoichiometric combustion occurs at a smaller radius ($r = 10$ mm). Due to the decrease in n-hexane concentration with increasing axial distance, more oxygen is entrained in the radial direction in the inner part of the luminous flame contour ($r = 10$ mm) where complete combustion occurs. The position of the luminous flame contour ($r = 12$ mm) is located outside of the position of the stoichiometric equivalence ratio.

At $x = 150$ mm, see Fig. 4(c), the luminous flame contour has an extension up to $r = 8$ mm, where the combustion processes are nearly complete and mostly turbulent mass transport phenomena occur. The main combustion products, such as CO_2 and H_2O, can be found in this plume zone. Here the species volume fractions have a minor effect on the specific refraction N_m as discussed below.

Figures 5(a) and 5(b) present axial species volume fractions profiles of the fuel, combustion products, and ambient air, measured by GC. Near the fuel surface, where high species volume fraction gradients occur, nitrogen concentrations are high (~18 vol.

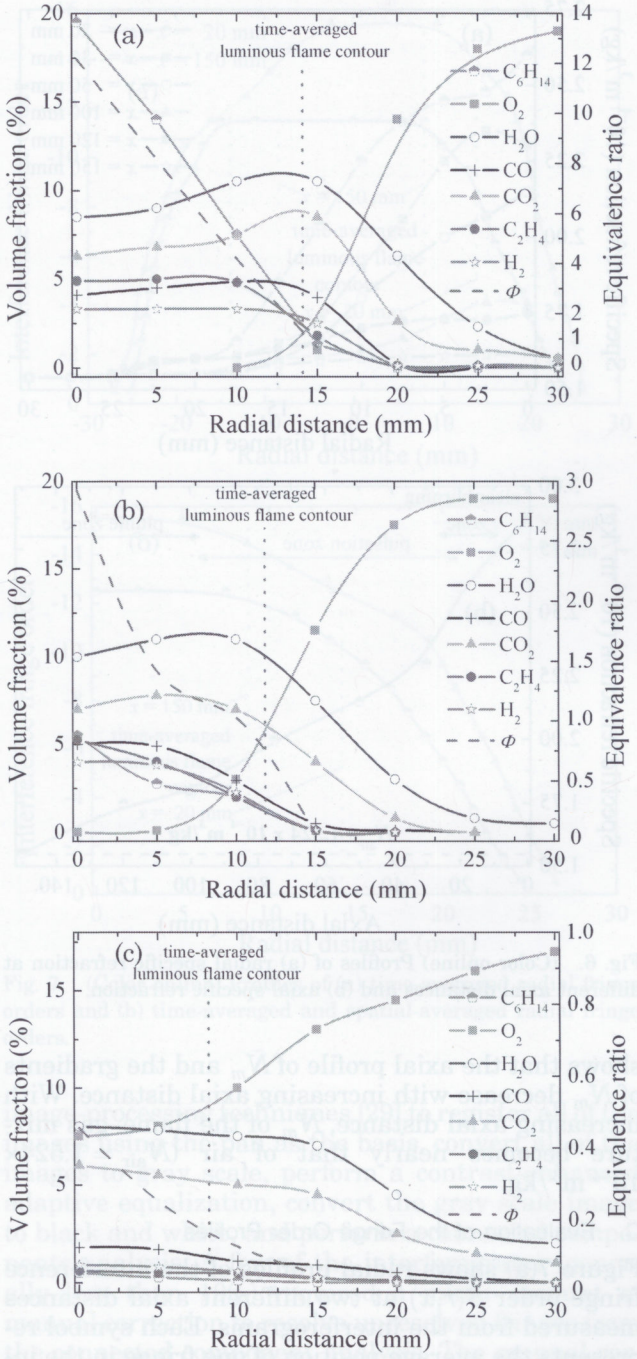

Fig. 4. (Color online) Profiles of radial species volume fractions and equivalence ratio at an axial distance of (a) $x = 20$ mm, (b) $x = 50$ mm, and (c) $x = 150$ mm.

%), indicating strong mixing of vaporizing fuel and ambient air. In addition, combustion products, such as H_2O, CO_2, and CO, can be found just above the fuel surface. Because of the relatively low temperature ($T = 383$ K) at this position, no n-hexane combustion takes place. The measured combustion products can only be explained by mixing phenomena caused by a recirculation zone near the tank rim. In the region $0\,\text{mm} < x < 80\,\text{mm}$, n-hexane is consumed up to a volume fraction of 1.5 vol. % [Fig. 5(a)]. All entrained oxygen is consumed within a thin flame zone [Figs. 4(a) and 4(b)], and no oxygen is able to penetrate into the inner region of the flame. At a height of $x > 60$ mm, the oxygen volume fraction begins to increase slightly (from 1 vol. % to 4.5 vol. %) at a height of $x = 80$ mm, whereas the nitrogen volume fraction has its largest decrease in the clear burning flame zone (from 67 vol. % to 18 vol. %). The axial volume fractions of the combustion products, H_2O, CO_2, and CO, increase with increasing axial distance [Fig. 5(b)] and have their maxima at a height of $x \approx 40$ mm ($\bar{\gamma}_{v,H_2O} = 12$ vol. %, $\bar{\gamma}_{v,CO_2} = 6.4$ vol. %, and $\bar{\gamma}_{v,CO} = 4.3$ vol. %). The plume zone of the flame contains mainly hot air with a small amount of combustion products and a larger quantity of soot. The remaining 1.5 vol. % of n-hexane is consumed (<0.5 vol. %) at a height of $x = 130$ mm, where the thermal boundary layer of the flame reaches its widest point. Within this region the oxygen volume fraction increases, from 4.5 to 9 vol. %, while the nitrogen volume fraction increases from 67 vol. % to 72 vol. %. The large increase in the oxygen volume fraction is due to the small concentration of combustible gases and the increasingly turbulent mixing process in this region. The main chemical reaction in the plume zone is the exothermic oxidation of CO to

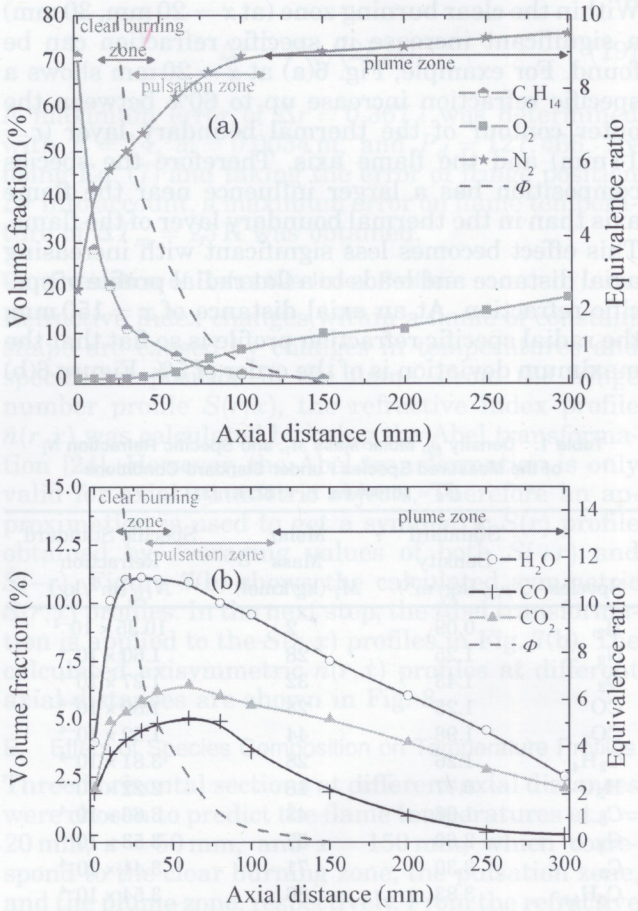

Fig. 5. (Color online) Profiles of axial species volume fractions of (a) fuel and ambient air N_2/O_2 and equivalence ratio and (b) major combustion products H_2O, CO_2, and CO.

generate CO_2. The volume fractions of the combustion products also decrease due to the increased mixing.

B. Influence of the Chemical Species Composition on Specific Refraction

From Eq. (3) it can be seen that the specific refraction N_m of the flame–gas mixture is influenced by the species composition. The specific refraction N_m can be calculated according to Eq. (4b). Table 1 contains some values of specific standard refraction for the selected measured species. Especially in the lower part of the flame, $x < 80$ mm, hydrocarbons from C_1 to C_6 can be found in higher volume fractions [Figs. 4(a) and 4(b)]. Hydrocarbons, H_2O, and H_2 have a higher standard refraction than O_2, N_2, CO_2, and CO. Table 1 shows that the hydroxyl radical and atomic nitrogen have large specific standard refractions $N_{i,0}$, but they are not considered because of their low concentrations (a maximum mole fraction of the order of $\bar{\gamma}_{v,OH} \approx 0.4$ vol. % for a nonpremixed flame [27]) and their small effect on refractivity of the flame–gas mixture. Therefore, neglecting these species will not affect N_m.

Figures 6(a) and 6(b) show radial and axial specific refraction profiles $\bar{N}_m$ calculated for the measured species volume fractions at different axial distances. Within the clear burning zone (at $x = 20$ mm, 30 mm) a significant increase in specific refraction can be found. For example, Fig. 6(a) at $x = 20$ mm shows a specific refraction increase up to 60% between the outer contour of the thermal boundary layer ($r = 14$ mm) and the flame axis. Therefore the species composition has a larger influence near the flame axis than in the thermal boundary layer of the flame. This effect becomes less significant with increasing axial distance and leads to a flat radial profile of specific refraction. At an axial distance of $x = 150$ mm, the radial specific refraction profile is so flat that the maximum deviation is of the order of 5%. Figure 6(b)

Table 1. Density ρ_i, Molar Mass M_i, and Specific Refraction N_i of the Measured Species i under Standard Conditions ($p_0 = 101000$ Pa, $T_0 = 273$ K) [31]

Species	Standard Density $\rho_{i,0}$ (kg/m^3)	Molar Mass M_i (kg/kmol)	Specific Standard Refraction $N_{i,0}$ (m^3/kg)
H_2	0.09	2	10.35×10^{-4}
N_2	1.25	28	1.60×10^{-4}
O_2	1.43	32	1.27×10^{-4}
CO	1.25	28	1.80×10^{-4}
CO_2	1.98	44	1.52×10^{-4}
C_2H_4	1.26	28	3.81×10^{-4}
H_2O	0.77	18	2.22×10^{-4}
C_{3-}	1.96	43	3.66×10^{-4}
C_{4-}	2.60	57	3.53×10^{-4}
C_{5-}	3.30	71	3.41×10^{-4}
C_6H_{14}	3.83	86	3.54×10^{-4}
O		16	1.80×10^{-4}
OH		17	3.50×10^{-4}
N		14	3.10×10^{-4}

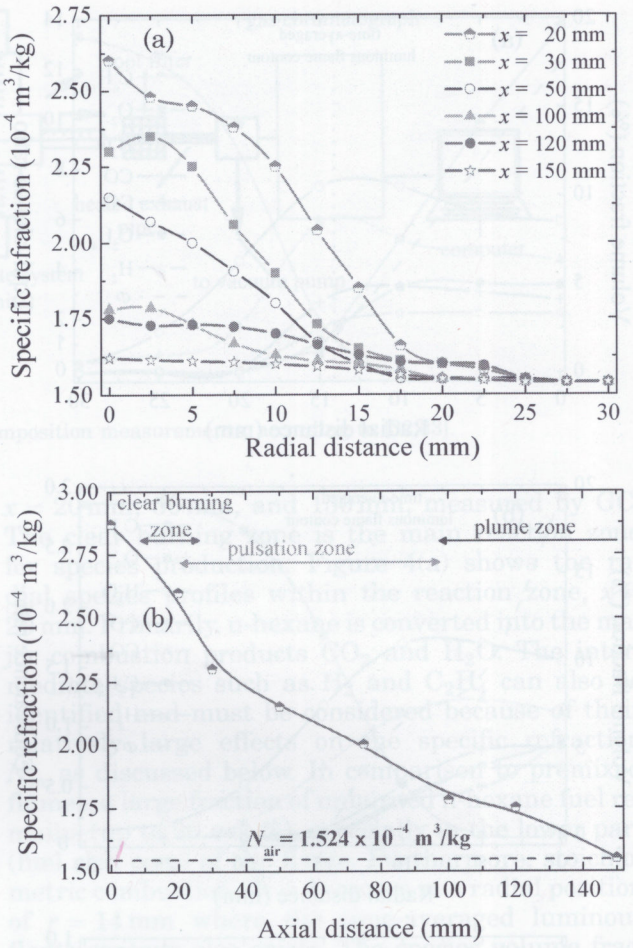

Fig. 6. (Color online) Profiles of (a) radial specific refraction at different axial distances and (b) axial specific refraction.

shows that the axial profile of $\bar{N}_m$ and the gradients of $\bar{N}_m$ decrease with increasing axial distance. With increasing axial distance, $\bar{N}_m$ of the flame–gas mixture becomes nearly that of air ($N_{air} = 1.524 \times 10^{-4}$ m^3/kg.

C. Evaluation of the Fringe Order Profiles

Figure 7(a) shows radial profiles of the interference fringe order $\bar{S}(r,x)$ at two different axial distances measured from the interferograms. Each symbol represents the average position of one fringe in the interferogram for 1000 images (every second image was analyzed), corresponding to a flow time of 4 s. Clearly the total number of fringes increases with increasing axial distance. The increased number of fringes with axial distance is due to the increasing number of sinks and sources, which causes additional fringes, especially in the plume zone. In addition, the flame is more symmetric in the lower part of the flame and becomes more asymmetric in the plume zone. In the region of the thermal boundary layer, a high number of interference fringes can be seen due to the high temperature gradients.

An inhouse MATLAB code was used to analyze the interferograms and determine the fringe order profiles. This code employed standard

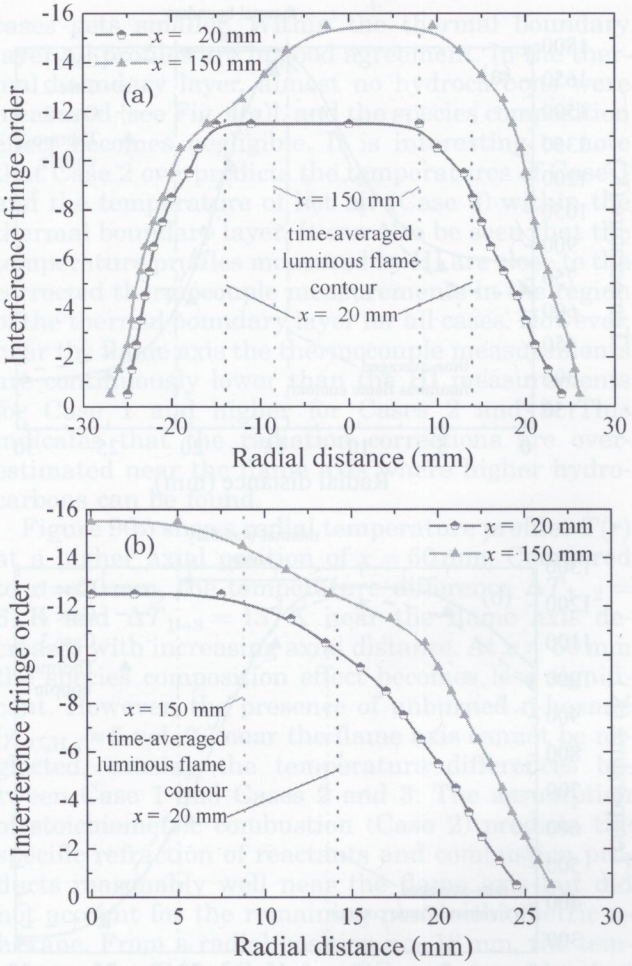

Fig. 7. (Color online) Profiles of (a) time-averaged radial fringe orders and (b) time-averaged and spatial-averaged radial fringe orders.

image-processing techniques [29] to register all of the images using the pan as the basis, convert all of the images to gray scale, perform a contrast-enhanced adaptive equalization, convert the gray scale image to black and white, and perform a connected components analysis. A few of the interferograms (generally less than 10%) required a minor amount of manual correction to resolve unresolved fringes from the connected component analysis. The manual correction involved comparing the original image with the connected-component image and adding or removing a few pixels from the connected-component image so as to create a continuous fringe that corresponded to the original image. For each interferogram, the connected component analysis numbered the fringes from left to right sequentially; these connected component numbers were then converted to fringe order number, which provided the fringe order profiles. A total of 1000 interferograms were analyzed using this method, which corresponds to approximately 20 puff cycles.

To determine the limits on the accuracy of the fringe positions, a sensitivity analysis was performed. The threshold values and the contrast-enhanced adaptive equalization limits were varied within the MATLAB code to determine the sensitivity of the interference fringe positions. The threshold values were varied by 15%, and the clip limit in the contrast-enhanced adaptive equalization function was varied by 20%. As in Jones *et al.* [30], the maximum error for fringe position Δr is given in relation to the sampling interval for the scan direction ΔL,

$$\Delta r = \Delta L/2. \tag{16}$$

This sampling interval for the scan direction is approximated using the length of a scan L_s and the total number of data points per scan P_d. The length of scan is approximated by the number of interference fringes F and the distance w between them:

$$\Delta L = L_s/P_d, \tag{17}$$

$$L_s = Fw. \tag{18}$$

Combining Eqs. (17)–(19) and converted to express the relative error for fringe position in quantities of wavelength can be determined by

$$\Delta r = Fw/(2P_d\lambda). \tag{19}$$

A maximum error of $\Delta r = 0.367\,\lambda$ was determined with $F = 14$, $w = 0.0034$ m, and $P_d = 127,466$. By using Eq. (7) and taking the error of fringe position Δr into account, a maximum error on flame temperature of $\Delta T_m = 25$ K was obtained.

D. Evaluation of Refractive Index Profiles

Refractive index changes within a flame of constant shape are caused by changes in temperatures and species composition in the flame. From the fringe number profile $\bar{S}(r,x)$, the refractive index profile $\bar{n}(r,x)$ was calculated by using the Abel transformation [24]. However, the Abel transformation is only valid for axial symmetric objects. Therefore an approximation is used to get a symmetric $\bar{S}(r)$ profile obtained by averaging values of both $\bar{S}(+r)$ and $\bar{S}(-r)$. Figure 7(b) shows the calculated symmetric $\bar{S}(r,x)$ profiles. In the next step, the Abel transformation is applied to the $\bar{S}(r,x)$ profiles in Fig. 7(b). The calculated axisymmetric $\bar{n}(r,x)$ profiles at different axial distances are shown in Fig. 8.

E. Effect of Species Composition on Temperature Profiles

Three horizontal sections at different axial distances were chosen to predict the flame temperatures at $x = 20$ mm, $x = 50$ mm, and $x = 150$ mm, which correspond to the clear burning zone, the pulsation zone, and the plume zone, respectively. From the refractive index profiles $\bar{n}(r,x)$, the temperature profiles $\bar{T}(r,x)$ were predicted using the relationship in Eq. (6). In order to study the effects of species composition

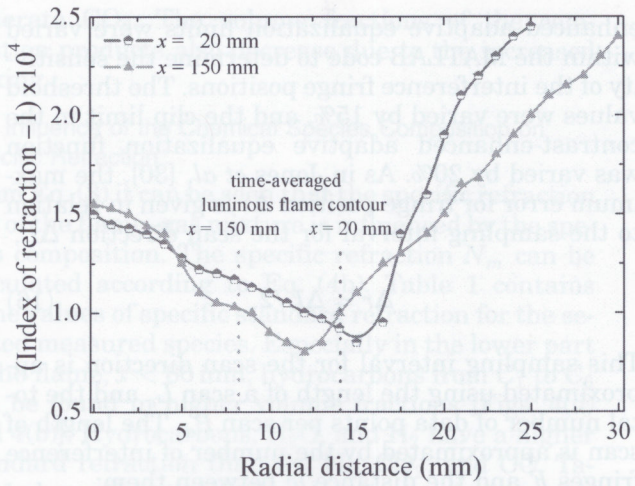

Fig. 8. (Color online) Profiles of time-averaged radial refractive index at $x = 20$ mm and $x = 150$ mm.

[second term of Eq. (6), right-hand side], the following three cases are considered.

Case 1: Using the measured $\bar{N}_m(r,x)$ profiles.

Case 2: Using a constant value of $\bar{N}_m$ based on stoichiometric combustion:

$$C_6H_{14} + 9.5(O_2 + 3.76N_2) \rightarrow 6CO_2 + 7H_2O + 35.72N_2. \quad (20)$$

Equation (20) shows the overall reaction mechanism and assumes that all the oxygen and fuel react to generate CO_2 and H_2O and that nitrogen does not. The specific refraction $\bar{N}_{m,R}$ of the reactants R is based on the assumption of complete combustion: $\bar{N}_{m,R} = 1.668 \times 10^{-4}\ m^3/kg$.The specific refraction $\bar{N}_{m,P}$ of the products P is based on the assumption of complete combustion:

$$\bar{N}_{m,P} = 1.641 \times 10^{-4}\ m^3/kg.$$

Averaged over reactants and products, $\bar{N}_m = (\bar{N}_{m,R} + \bar{N}_{m,P})/2 = 1.655 \times 10^{-4}\ m^3/kg$.

Case 3: Assuming that flame consists of hot air, $\bar{N}_m = N_{air} = 1.532 \times 10^{-4}\ m^3/kg$.

Figure 9(a) shows radial temperature profiles $\bar{T}(r)$ at an axial position of $x = 20$ mm for the three cases. It also shows that the temperature increases rapidly within the thermal boundary layer until reaching a maximum temperature of $\bar{T} = 1760$ K. The maximum temperature exists near the visible flame contour at a radial position of $r = 14$ mm and decreases with decreasing radial distance. The maximum temperature occurs at a slightly fuel rich condition $\phi = 1.1$ [Fig. 4(a)]. This might be due to mixing processes (entrainment of ambient air) causing slightly higher oxygen concentrations. Temperature differences $\Delta\bar{T}_{1\rightarrow2} = 150$ K and $\Delta\bar{T}_{1\rightarrow3} = 230$ K, respectively, are found near the flame axis where the n-hexane volume fractions ($\bar{\gamma}_{v,C_6H_{14}} \approx 20$ vol. %) are high. Here, the effect of species composition and refractivity is the greatest where a large amount of

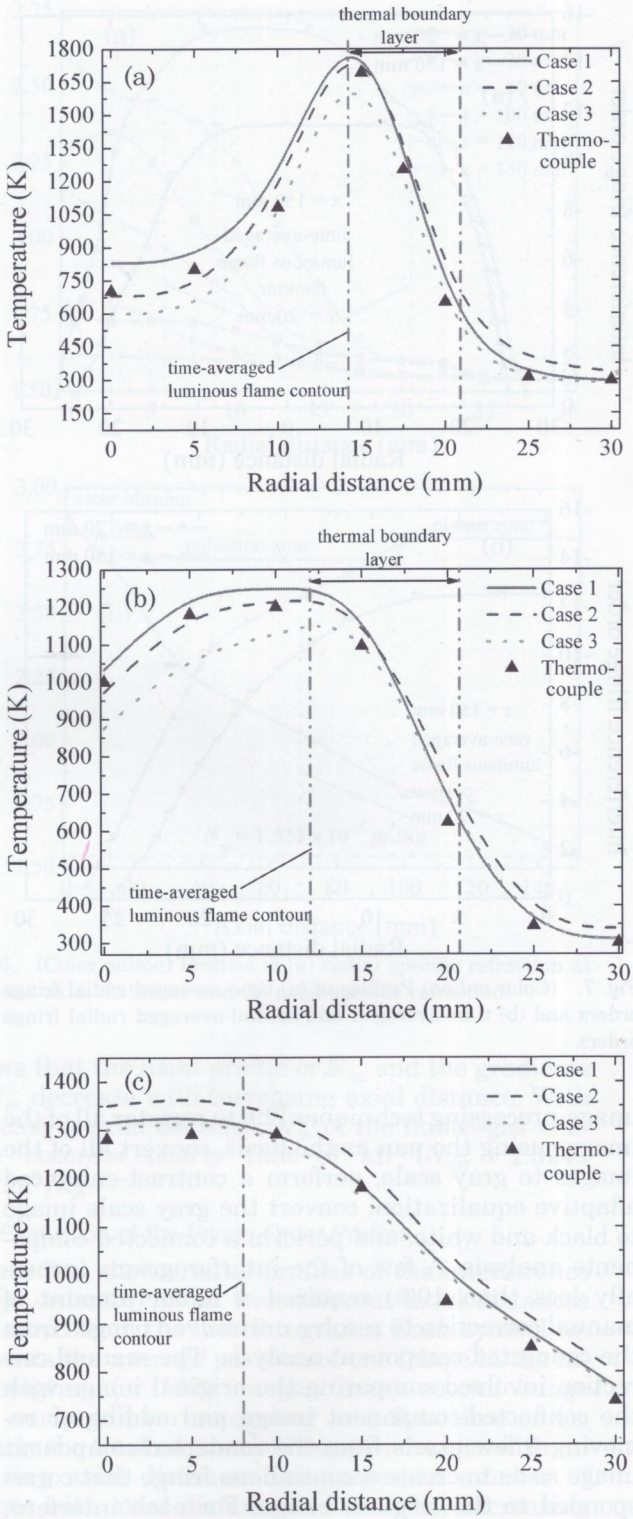

Fig. 9. (Color online) Profiles of time-averaged radial temperatures at (a) $x = 20$ mm, (b) $x = 50$ mm, and (c) $x = 150$ mm by considering N_m calculated with the measured species composition (Case 1), an average value of stoichiometric combustion (Case 2) and a constant value of air (Case 3).

higher hydrocarbons (with a high specific standard refraction) can be found [Fig. 4(a)]. A different situation exists with increasing radial distance $r > 16$ mm where the temperature difference between the three

cases gets smaller. Within the thermal boundary layer all profiles are in good agreement. In the thermal boundary layer, almost no hydrocarbons were measured [see Fig. 4(a)], and the species composition effect becomes negligible. It is interesting to note that Case 2 overpredicts the temperatures of Case 1 and the temperature of hot air (Case 3) within the thermal boundary layer. It can also be seen that the temperature profiles measured by HI are close to the corrected thermocouple measurements in the region of the thermal boundary layer for all cases. However, near the flame axis the thermocouple measurements are continuously lower than the HI measurements for Case 1 and higher for Cases 2 and 3. This indicates that the radiation corrections are overestimated near the flame axis where higher hydrocarbons can be found.

Figure 9(b) shows radial temperature profiles $\bar{T}(r)$ at a higher axial position of $x = 50\,\text{mm}$. Compared to $x = 20\,\text{mm}$, the temperature difference $\Delta\bar{T}_{1\to2} = 61\,\text{K}$ and $\Delta\bar{T}_{1\to3} = 137\,\text{K}$ near the flame axis decreases with increasing axial distance. At $x = 50\,\text{mm}$ the species composition effect becomes less significant. However, the presence of unburned n-hexane ($\bar{\gamma}_{v,C_6H_{14}} \approx 5$ vol. %) near the flame axis cannot be neglected, causing the temperature differences between Case 1 and Cases 2 and 3. The assumption of stoichiometric combustion (Case 2) predicts the specific refraction of reactants and combustion products reasonably well near the flame axis but did not account for the remaining nonstoichiometric n-hexane. From a radial position $r > 18\,\text{mm}$, the temperature profiles of Case 1 and Case 3 show identical trends and are nearly indistinguishable. Again, Case 2 overpredicts the temperatures of Case 1 and the temperatures of hot air (Case 3) within the thermal boundary layer. Temperatures measured by HI for Cases 1 and 2 are in good agreement with the thermocouple measurements.

At an axial position of $x = 150\,\text{mm}$ [Fig. 9(c)], Case 2 consistently overestimates the flame temperatures compared with Cases 1 and 3. Here, the dominant combustion process is the oxidation of CO to generate CO_2 [Fig. 4(c)], and the temperature profile cannot be adequately represented by the overall reaction mechanism. A satisfactory approximation is the assumption of hot air that leads to the good agreement of the temperature profiles between Case 1 and Case 3 across all radial coordinates. With reasonable temperature corrections, temperature profiles measured by thermocouples agree with the interferometric temperatures for Cases 1 and 3. Also, it can be seen that the differences in measured temperatures between the HI method and the thermocouples decrease as the axial coordinate increases. Temperature differences between these methods can occur because each temperature profile is independently measured by thermocouples and HI.

These analyses show that the predicted temperature profiles $\bar{T}(r,x)$ are sensitive to species composition near the flame axis, especially at lower axial distances ($x = 20\,\text{mm}$, $x = 50\,\text{mm}$). The species composition effect becomes less significant in the plume zone (e.g., $x = 150\,\text{mm}$) and within the thermal boundary layer where only temperature gradients exist.

5. Conclusions

From the results the following conclusions can be drawn:

1. The influence of the composition effect on temperature fields in tank fires depends on the mixing process between the flame gases and the entrained ambient air.
2. In the region of the clear burning zone, e.g., at $x = 20\,\text{mm}$, species composition has the largest effect on the temperature profiles near the flame axis $r < 10\,\text{mm}$ (fuel rich region), leading to a maximum temperature difference up to $\Delta\bar{T}_{\max} = 230\,\text{K}$ between the interferometric measured temperatures and the assumption of a uniform composition of hot air.
3. Within the thermal boundary, $r > 14$, mm the flame gases consist primarily of hot air independent of the axial distance.
4. In the region of the pulsation zone, e.g., $x = 50\,\text{mm}$, the species composition becomes less significant due to better mixing of entrained air and combustion products. The assumption of stoichiometric combustion, especially near the flame axis, is reasonable for predicting the temperatures near the flame axis. However, this assumption generally overpredicts the temperatures in the thermal boundary layer.
5. In the region of the plume zone, e.g., at $x = 150\,\text{mm}$, the composition of the flame gases can be assumed to consist primarily of hot air due to the increase in total entrained ambient air.

If the composition of the flame–gas mixture is unknown, a uniform composition of hot air can be assumed to predict temperature fields as measured by HI except in the region near the flame axis and at lower axial distances.

The collaboration and many helpful discussions with Eric G. Eddings, JoAnn S. Lighty, Adel F. Sarofim, Philip J. Smith, and Jennifer P. Spinti of the Institute for Clean and Secure Energy (ICSE), University of Utah, are greatly appreciated. In addition we would like to thank Henning Bockhorn, Institute for Technical Chemistry and Polymer Chemistry, University of Karlsruhe (TH), Germany, for his valuable collaboration. One of the authors (Markus Gawlowski) acknowledges the financial support from the Max-Buchner-Forschungsstiftung, DECHEMA, Frankfurt/Main, Germany.

References

1. M. Hailwood, M. Gawlowski, B. Schalau, and A. Schönbucher, "Conclusions drawn from the Buncefield and Naples incidents regarding the utilization of consequence models," Chem. Eng. Technol. **32**, 207–233 (2009).

2. T. L. Henriksen, T. A. Ring, E. G. Eddings, and G. J. Nathan, "Puffing frequency and soot extinction correlation in JP-8 and heptanes pool fires," Combust. Sci. Technol. **180**, 699–712 (2008).
3. L. Audouin, G. Kolb, J. L. Torero, and J. M. Most, "Average centreline temperatures of a buoyant pool fire obtained by image processing of video recordings," Fire Safety J. **24**, 167–187 (1995).
4. B. Arnold, V. Banhardt, V. Bieller, H. Kasper, M. Kaufmann, R. Lucas, and A. Schönbucher, "Simultaneous observation of organized density structures and the visible field in pool fires," in *Proceedings of 21th Symposium (Int.) on Combustion* (The Combustion Institute, 1986), pp. 83–92.
5. J. A. Qi, C. W. Leung, W. O. Wong, and S. D. Probert, "Temperature-field measurements of a premixed butane/air circular impinging-flame using reference-beam interferometry," Appl. Energy **83**, 1307–1316 (2006).
6. M. Gawlowski, M. Hailwood, I. Vela, and A. Schönbucher, "Deterministic and probabilistic estimation of appropriate distances: motivation for considering the consequences for industrial sites," Chem. Eng. Technol. **32**, 182–198 (2009).
7. S. M. Tieng, W. Z. Lai, and T. Fujiwara, "Holographic temperature measurement on axisymmetric propane-air, fuel-lean flame," Meas. Sci. Technol. **3**, 1179–1187 (1992).
8. R. A. Dobbins, "Soot inception temperature and the carbonization rate of precursor particles," Combust. Flame **130**, 204–214 (2002).
9. D. Y. Zhang and H. C. Zhou, "Temperature measurement by holographic interferometry for non-premixed ethylene-air flame with a series of state relationships," Fuel **86**, 1552–1559 (2007).
10. A. Stella, G. Guj, and S. Giammartini, "Measurement of axisymmetric temperature fields using reference beam and shearing interferometry for application to flames," Exp. Fluids **29**, 1–12 (2000).
11. J. Doi and S. Sato, "Three-dimensional modeling of the instantaneous temperature distribution in a turbulent flame using multidirectional interferometer," Opt. Eng. **46**, 015601 (2007).
12. C. Shakher and A. K. Nirala, "A review on refractive index and temperature profile measurements using laser-based interferometric techniques," Opt. Lasers Eng. **31**, 455–491 (1999).
13. S. M. Tieng, C. C. Lin, Y. C. Wang, and T. Fujiwara, "Effect of composition distribution on holographic temperature measurement of a diffuse flame," Meas. Sci. Technol. **7**, 477–488 (1996).
14. G. P. Montgomery and D. L. Reuss, "Effects of refraction on axisymmetric flame temperatures measured by holographic interferometry," Appl. Opt. **21**, 1373–1380 (1982).
15. C. C. Chen, K. C. Chang, and S. M. Tieng, "Effect of composition change on temperature measurements in a premixed flame by holographic interferometry," Opt. Eng. **31**, 353–362 (1992).
16. J. D. Posner and D. Dunn-Rankin, "Temperature field measurements of small, nonpremixed flames with use of an Abel inversion of holographic interferograms," Appl. Opt. **42**, 952–959 (2003).
17. T. Konishi, A. Ito, Y. Kudo, A. Narumi, K. Saito, J. Baker, and P. M. Struk, "Simultaneous measurement of temperature and chemical species concentrations with a holographic interferometer and infrared absorption," Appl. Opt. **45**, 5725–5732 (2006).
18. P. A. Ross and M. M. El-Wakil, "A two-wavelength interferometric technique for the study of vaporization and combustion of fuels," in *AIIA Progress in Astronautics and Rocketry: Liquid Rockets and Propulsion*, L. E. Bollinger, M. Goldsmith, and A. W. Lemmon, Jr., eds. (Academic, 1960), pp. 265–298.
19. T. Kreis, *Handbook of Holographic Interferometry* (Wiley-VCH, 2005).
20. W. Hauf and U. Grigull, "Optical methods in heat transfer," in *Advances in Heat Transfer*, J. P. Hartnett and T. F. Irvine Jr., eds. (Academic, 1970), Vol. 6, pp. 267–274.
21. C. M. Vest, "Interferometry of strongly refracting axisymmetric objects," Appl. Opt. **14**, 1601–1606 (1975).
22. R. Lucas, "Holografische Synchroninterferometrie zur Untersuchung von Tankflammenfeldern und ihren kohärenten Strukturen," Ph.D. thesis (University of Stuttgart, 1981).
23. D. L. Reuss, "Temperature measurements in a radially symmetric flame using holographic interferometry," Combust. Flame **49**, 207–219 (1983).
24. C. M. Vest, *Holographic Interferometry* (Wiley, 1979).
25. W. Hauf, U. Grigull, and F. Mayinger, *Optische Meßverfahren der Wärme- und Stoffübertragung* (Springer, 1991).
26. A. F. Ibarreta and C.-J. Sung, "Flame temperature and location measurements of sooting premixed Bunsen flames by rainbow schlieren deflectometry," Appl. Opt. **44**, 3565–3575 (2005).
27. M. D. Smooke, Y. Xu, R. M. Zurn, P. Lin, J. H. Frank, and M. B. Long, "Computational and experimental study of OH and CH radicals in axisymmetric laminar diffusion flames," in *Proceedings of 24th Symposium (Int.) on Combustion* (The Combustion Institute, 1992), pp. 813–821.
28. R. Fristrom and A. Westenberg, *Flame Structure* (McGraw-Hill, 1965).
29. R. C. Gonzalez, R. E. Woods, and S. L. Eddins, *Digital Image Processing Using Matlab* (Pearson Prentice Hall, 2004).
30. R. A. Jones and P. L. Kadakia, "An automated interferogram analysis technique," Appl. Opt. **7**, 1477–1482 (1968).
31. W. C. Gardiner, Y. Hidaka, and T. Tanzawa, "Refractivity of combustion gases," Combust. Flame **40**, 213–219 (1981).
32. A. Walcher, "Nicht-isothermer Stofftransport und Reaktionsräume in Tankflammen," Ph.D. thesis (University of Stuttgart, 1982).
33. W. Brötz, A. Walcher, and A. Schönbucher, "Gaschromatographische Analyse der Flammengase einer n-Hexan-Tankflamme," Erdöl-Kohle-Erdgas-Petrochem. **31**, 347–353 (1978).